nature nanotechnology

LETTERS

PUBLISHED ONLINE: 19 JANUARY 2014 | DOI: 10.1038/NNANO.2013.286

A nanophotonic solar thermophotovoltaic device

Andrej Lenert[1], David M. Bierman[1], Youngsuk Nam[1,4], Walker R. Chan[2,3], Ivan Celanović[3], Marin Soljačić[2,3] and Evelyn N. Wang[1]*

The most common approaches to generating power from sunlight are either photovoltaic, in which sunlight directly excites electron–hole pairs in a semiconductor, or solar-thermal, in which sunlight drives a mechanical heat engine. Photovoltaic power generation is intermittent and typically only exploits a portion of the solar spectrum efficiently, whereas the intrinsic irreversibilities of small heat engines make the solar-thermal approach best suited for utility-scale power plants. There is, therefore, an increasing need for hybrid technologies for solar power generation[1,2]. By converting sunlight into thermal emission tuned to energies directly above the photovoltaic bandgap using a hot absorber–emitter, solar thermophotovoltaics promise to leverage the benefits of both approaches: high efficiency, by harnessing the entire solar spectrum[3–5]; scalability and compactness, because of their solid-state nature; and dispatchablility, owing to the ability to store energy using thermal or chemical means[6–8]. However, efficient collection of sunlight in the absorber and spectral control in the emitter are particularly challenging at high operating temperatures. This drawback has limited previous experimental demonstrations of this approach to conversion efficiencies around or below 1% (refs 9–11). Here, we report on a full solar thermophotovoltaic device, which, thanks to the nanophotonic properties of the absorber–emitter surface, reaches experimental efficiencies of 3.2%. The device integrates a multiwalled carbon nanotube absorber and a one-dimensional Si/SiO_2 photonic-crystal emitter on the same substrate, with the absorber–emitter areas optimized to tune the energy balance of the device. Our device is planar and compact and could become a viable option for high-performance solar thermophotovoltaic energy conversion.

Because no portion of incident sunlight reaches the photovoltaic cell directly, the performance of solar thermophotovoltaics (STPVs) relies on the efficiency of several intermediate energy conversion steps. Optically concentrated sunlight is converted into heat in the absorber, the absorber temperature rises, heat conducts to the emitter, and the hot emitter thermally radiates towards the photovoltaic cell, where radiation is ultimately harnessed to excite charge carriers and generate power (Fig. 1a). The overall efficiency η_{stpv} can be expressed as a product of the optical efficiency of concentrating sunlight (η_o), the thermal efficiency of converting and delivering sunlight as heat to the emitter (η_t), and the efficiency of generating electrical power from the thermal emission (η_{tpv}):

$$\eta_{stpv} = \eta_o \eta_t \eta_{tpv}$$

The thermophotovoltaic (TPV) efficiency η_{tpv} hinges on the spectral properties and temperature of the emitter. A spectrally selective emitter should have high emittance for energies above the photovoltaic bandgap (E_g) and low emittance for energies below the bandgap. To excite enough thermal modes for substantial emission above the bandgap, the emitter temperature should ideally[12] be high enough that Planck's blackbody peak coincides with the bandgap; in other words, by Wien's displacement law,

$$T_e^{opt} \approx 2336\,[\mathrm{K\ eV^{-1}}] \cdot E_g$$

The high-temperature operation of the emitter poses two key challenges to efficient STPV power conversion: collecting sunlight to efficiently reach T_e^{opt} and maintaining spectral selectivity at elevated temperatures. Past STPV embodiments have relied on the intrinsic properties of materials such as tungsten[9,10]. For the absorber, one approach to effectively enhance the intrinsic solar absorptivity of materials is to use macro-cavity geometries. Because of the high aspect ratio of the cavity needed to enhance absorption, this approach typically requires high levels of optical concentration to reach T_e^{opt} (for example, 3,183 times, as used by Datas and Algora[9], and 4,600 times, as used by Vlasov *et al.*[10]). Such a high optical concentration in turn requires complex systems with relatively low optical efficiencies ($\eta_o \approx 65\%$)[9]. For the emitter, the intrinsic spectral selectivity of tungsten is poor at T_e^{opt} because the emissivity at low photon energies ($<E_g$) increases with temperature, accompanying an increase in electrical resistivity[13]. Ultimately, the reliance on the intrinsic spectral properties of materials for the absorber–emitter has limited previously reported experimental STPVs to conversion efficiencies around 1% (refs 9–11).

To improve the performance of the absorber–emitter, researchers have investigated the design of structured surfaces[5,6,14–21] with spectral properties approaching those of ideal STPV components (specifically, the use of photonic crystals to control the photon density of states for narrow-band selective emission[5,6,14–20]). Simulation studies using realistic nanophotonic surfaces predict STPV efficiencies exceeding 40% (refs 5,15,21). Although the intrinsic material properties are sensitive to temperature, the surface structure affords a degree of spectral tunability that is temperature-independent. Nevertheless, these surfaces have not yet been integrated into STPV devices operating at high enough temperatures for efficient power conversion.

In our device, the spectral properties of the absorber–emitter are tailored through surface nanostructuring in a compact planar layout (Fig. 1a,b). The absorber–emitter module is composed of an array of multiwalled carbon nanotubes (MWNTs) as the solar absorber and a one-dimensional Si/SiO_2 photonic crystal (1D PhC) as the selective emitter. We varied the emitter-to-absorber area ratio ($AR = A_e/A_a$) from 1 to 10 to achieve optimal performance. With increasing area ratio, we supply enough heat for the absorber–emitter to reach T_e^{opt} by increasing the level of irradiance and leveraging the high absorptance of the nanotube array. Thermal

[1]Device Research Laboratory, Department of Mechanical Engineering, Massachusetts Institute of Technology, 77 Massachusetts Avenue, Cambridge, Massachusetts 02139, USA, [2]Research Laboratory of Electronics, Massachusetts Institute of Technology, 77 Massachusetts Avenue, Cambridge, Massachusetts 02139, USA, [3]Institute for Soldier Nanotechnology, Massachusetts Institute of Technology, 77 Massachusetts Avenue, Cambridge, Massachusetts 02139, USA, [4]Department of Mechanical Engineering, Kyung Hee University, Yongin 446-701, Korea. *e-mail: enwang@mit.edu

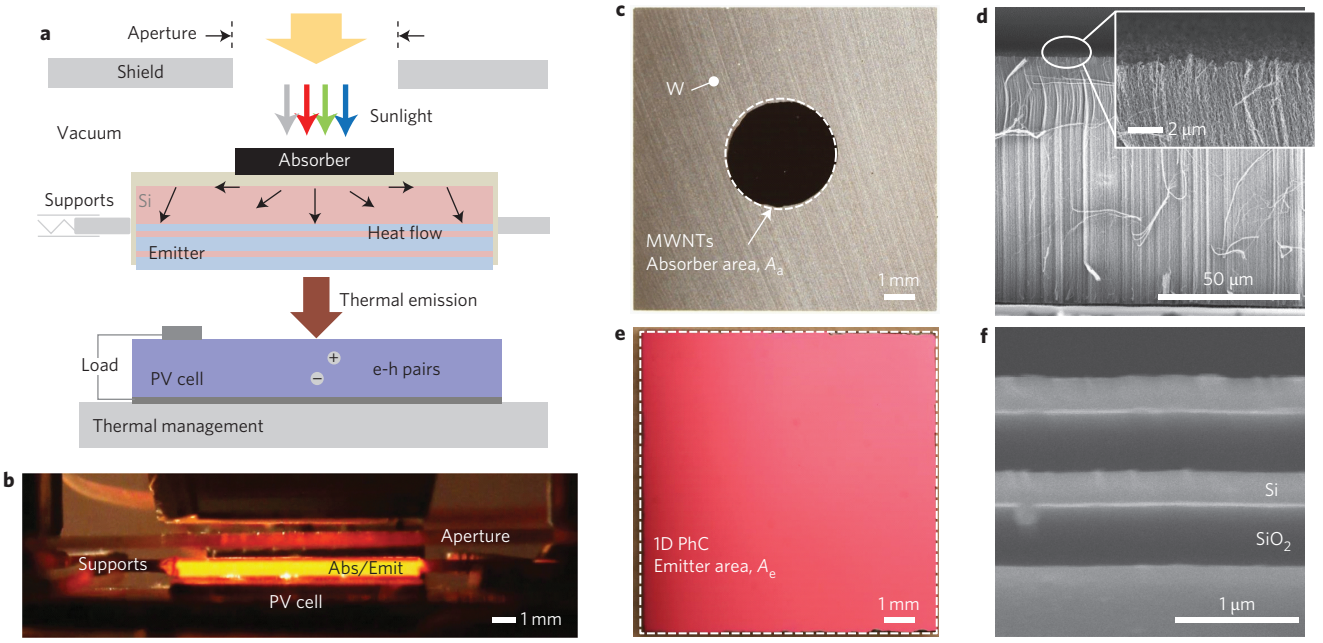

Figure 1 | Operating principle and components of the NARO-STPV. Sunlight is converted into useful thermal emission and, ultimately, electrical power, via a hot absorber–emitter. **a**,**b**, Schematic (**a**) and optical image (**b**) of our vacuum-enclosed devices composed of an aperture/radiation-shield, an array of MWNTs as the absorber, a 1D PhC, a 0.55 eV-bandgap photovoltaic cell (InGaAsSb[19–21]) and a chilled water cooling system. **c**, Absorber-side optical image of an AR ($=A_e/A_a$) $=10$ module showing spatially defined MWNTs ($A_a = 0.1$ cm^2) on a tungsten-coated silicon substrate (1×1 cm^2 planar area, 550 μm thick). **d**, SEM cross-section of the MWNTs. Inset: Magnified view of the nanotube tips. **e**, Optical image of the 1D PhC emitter ($A_e = 1$ cm^2). **f**, SEM cross-section of the 1D PhC showing the alternating layers of silicon and SiO_2.

resistance between the absorber and emitter is minimized by integrating the absorber and emitter on the same conductive silicon substrate such that heat is effectively delivered to the emitter via thermal spreading. Because the absorber area is reduced with respect to the planar area of the sample (Fig. 1c), the area for re-emissive losses from the nearly blackbody nanotube array surface is decreased, thus boosting thermal efficiency. To reduce parasitic radiative losses, we metallized the sides of the silicon substrate and inactive area around the nanotube absorber with tungsten, a relatively low-emissivity, high-temperature material, and incorporated a high-reflectivity silver-coated shield (Fig. 1a) to recycle this parasitic radiation back to the device.

Vertically aligned carbon nanotubes were chosen as the solar absorber because of their high-temperature stability in vacuum and their nearly ideal absorptance, crucial for absorbing highly concentrated irradiance at elevated emitter-to-absorber area ratios. As shown in Fig. 1d, the as-grown nanotubes are 10–15 nm in outer diameter and 80–100 μm tall, with an ~0.5 μm variation in height at the tips. The broad–spectrum absorptance of the nanotube array in this study exceeds 0.99 (Supplementary section 'Absorber characterization'), consistent with previous reports for similar nanotube array geometries[22–24].

The multilayer Si/SiO_2 structure of the photonic crystal, composed of five alternating layers of silicon and SiO_2 (Fig. 1e,f), improves the spectral matching between the emittance of the emitter and the internal quantum efficiency of the InGaAsSb photovoltaic cell[25–27] ($E_g = 0.55$ eV). These materials were chosen for ease of fabrication and high-temperature compatibility with the silicon substrate. The layer thicknesses were optimized via a constrained global optimization of the product of efficiency and power density[6].

Our mechanical system ensures alignment and gap control while minimizing parasitic conduction losses (Supplementary section 'Experimental set-up'). The entire experimental layout was maintained in vacuum (<0.5 Pa) to suppress convective and conductive heat transfer through the environment. We used a xenon-arc light source to simulate the solar spectrum and to supply a range of irradiances H_s from 10 to 75 W cm^{-2}.

To gain more insight into the complex energy conversion in our nanophotonic area-ratio optimized (NARO) STPV devices and compare it to theoretical predictions, we conducted two

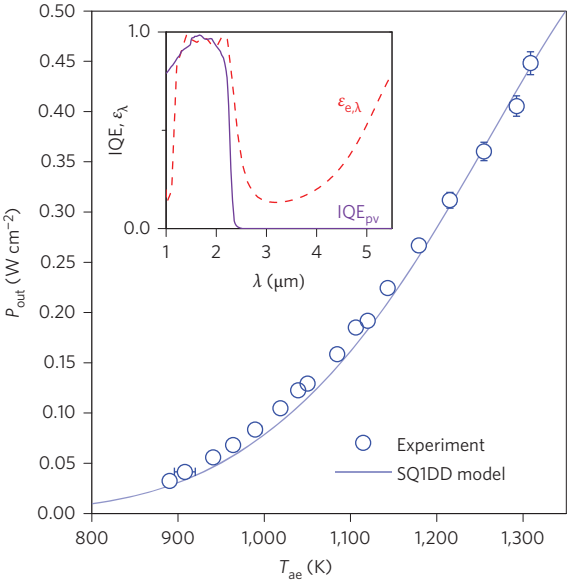

Figure 2 | TPV characterization. Electrical output power density (P_{out}) generated by the InGaAsSb photovoltaic cell as a function of the 1D Si/SiO_2 PhC emitter temperature. Inset: Measured[4] spectral emittance ($\varepsilon\lambda$) of the 1D PhC at 1,285 K and the internal quantum efficiency (IQE) of the photovoltaic used by the SQ1DD model. The model prediction (solid line) shows excellent agreement with experimental points (symbols). Error bars represent 95% confidence interval (see Methods).

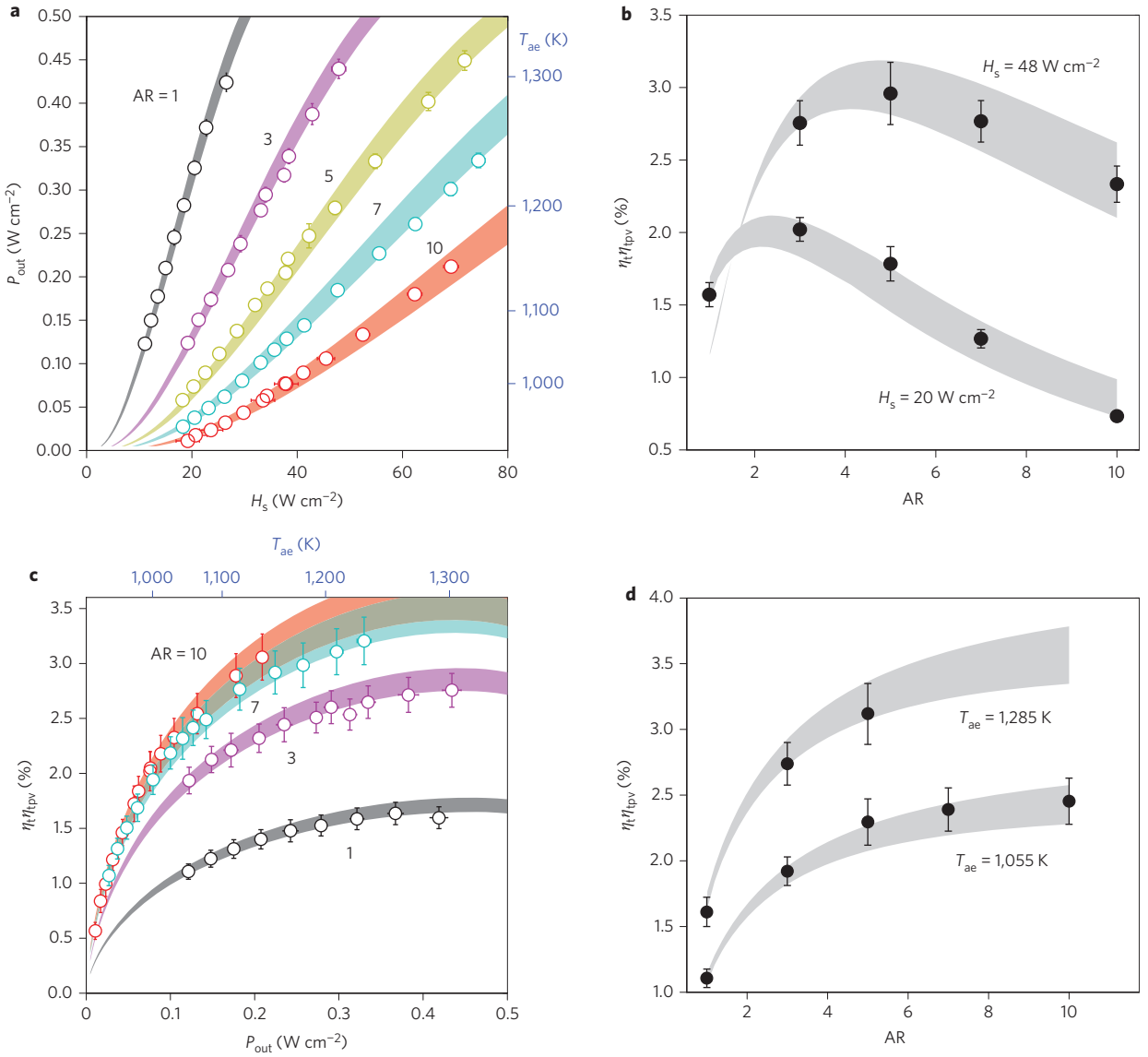

Figure 3 | Performance characterization and optimization of the nanophotonic STPV device. a, Electrical output power density (P_{out}) and absorber–emitter temperature (T_{ae} determined from Fig. 2) with increasing H_s (input solar power normalized by the aperture area) for AR = 1 to 10. As the area ratio is increased, the device operates in a regime of decreased $\sigma T_{ae}^4/H_s$, which is favourable for the absorber efficiency of the nanotube array. **b**, Conversion efficiency (concentrated solar to electrical, $\eta_t\eta_{tpv}$) with increasing area ratio for fixed $H_s = 20$ and 48 W cm^{-2}. Competing effects of the thermal efficiency and the TPV efficiency lead to an optimal area ratio for a fixed H_s. **c**, Conversion efficiency as a function of P_{out} or, equivalently, T_{ae} (AR = 5 omitted for clarity). **d**, At a given P_{out} or T_{ae}, the conversion efficiency increases with increasing area ratio, which is attributed to an increase in thermal efficiency. Markers are experimental points (error bars represent 95% confidence interval; see Methods) and solid bands represent the SQ1DD model, treating H_s as collimated or diffuse sets the upper and lower bounds, respectively.

independent experiments: TPV and STPV. We investigated the maximum output power density (P_{out}) of the photovoltaic diode as a function of the absorber–emitter temperature T_{ae} in the TPV experiment, and irradiance H_s in the STPV experiment. The temperature measurement in the TPV characterization was achieved by bonding a fine-gauge thermocouple directly to the absorber side of the substrate.

As shown in Fig. 2, the output power of the photovoltaic cell is highly temperature-dependent, as higher energy modes ($>E_g$) are excited with increasing emitter temperature. These experimental results are supported by a spectral quasi-1D diffuse radiative network model (SQ1DD). Our model assumes isothermal operation of the absorber–emitter (that is, $T_a = T_e = T_{ae}$) and accounts for the experimentally measured spectral properties of the components and the geometrical configuration of our planar STPV layout (Supplementary section 'Modelling'). The results of the TPV experiment serve as validation of our model and provide an indirect method for determining the absorber–emitter temperature from the measured output power. This approach was used in the STPV characterization because a direct *in situ* measurement of the absorber–emitter temperature increases parasitic losses and reduces efficiency.

With the TPV performance characterized, we investigated the full energy conversion processes in our NARO–STPVs with increasing emitter-to-absorber area ratios. Figure 3a shows the electrical output power of the STPV devices as a function of irradiance H_s and absorber–emitter temperature (determined using the relation between P_{out} and T_{ae} shown in Fig. 2). The upper and lower

estimates of our SQ1DD model (associated with treating H_s as collimated or diffuse, respectively) bound the data within the experimental uncertainty.

The effect of increasing area ratio is manifested in shifting the operating points to a regime of increased irradiance H_s relative to the thermal re-emission loss (σT_{ae}^4). If we consider the absorber solar collection efficiency (a major component of the thermal efficiency) for a blackbody surface

$$\eta_a^{BB} = 1 - \frac{\sigma T_{ae}^4}{H_s} \quad (1)$$

we observe that decreasing the $\sigma T_{ae}^4/H_s$ ratio results in higher absorber efficiency (σ is the Stefan–Boltzmann constant). For our nearly blackbody nanotube absorbers, this regime corresponds graphically to the lower right corner of Fig. 3a. Using equation (1), we estimated that the absorber efficiency for AR = 10 is above 75%.

Nevertheless, absorber efficiency is only a component of the overall STPV efficiency. Indeed, the efficiency of converting concentrated sunlight into electrical power ($\eta_t\eta_{tpv}$) does not monotonically increase with increasing area ratio for a fixed irradiance H_s. As shown in Fig. 3b, an optimal area ratio exists. To understand why this optimal area ratio arises, the competing effects of the thermal efficiency and the TPV efficiency are considered. The thermal efficiency is significantly enhanced as the area ratio increases due to a rise in absorber efficiency (as explained above). In contrast, with increasing area ratio for fixed H_s, the operating temperature of the absorber–emitter decreases because the ratio of the absorbed solar power ($\sim A_a H_s$) relative to the thermal emission ($\sim A_e \sigma T_{ae}^4$) decreases, ultimately leading to a decrease in TPV efficiency as the temperature drops significantly below T_e^{opt}. These two competing effects lead to an optimal area ratio for a fixed irradiance or, equivalently, for a fixed optical concentration (10 times = 1 W cm^{-2}, ASTM E772). In general, the optimum area ratio increases with optical concentration, as shown in Fig. 3b, where the optimum shifts from approximately AR = 2 to AR = 5 as H_s increases from 20 to 48 W cm^{-2}.

Using the relation between P_{out} and T_{ae} (Fig. 2), we investigated the system performance as a function of absorber–emitter temperature. Figure 3c shows that the efficiency initially increases sharply with emitter temperature (below 1,200 K) as modes with energies above E_g are increasingly excited. As the temperature approaches T_e^{opt}, the efficiency plateaus as increasing useful emission (that is, radiation at $E > E_g$) is balanced by increasing re-emission losses and photovoltaic inefficiencies associated with high photocurrents. Increasing the area ratio for a given absorber–emitter temperature results in increased conversion efficiency (Fig. 3d). Because the TPV efficiency is determined by the emitter temperature, the relative increase in conversion efficiency ($\eta_t\eta_{tpv}$) is completely attributed to the increase in thermal efficiency. At T_e^{opt} (1,285 K), we experimentally demonstrated a twofold increase in thermal efficiency from AR = 1 to AR = 5.

Overall, the highest conversion efficiency ($\eta_t\eta_{tpv}$) that we measured was 3.2 ± 0.2% using an AR = 7 device, which is three times greater than that obtained in previous STPV experiments[9]. This was achieved using a compact design at substantially lower levels of optical concentration (~750 times), which enables higher optical efficiencies. As shown in Fig. 4, significant enhancements in efficiency relative to a greybody absorber–emitter ($\varepsilon = 0.5$) were achieved through the use of (1) a 1D PhC for improved spectral performance of the emitter and a vertically aligned MWNT array for nearly ideal solar absorptance (a twofold contribution to the improvement in $\eta_t\eta_{tpv}$) and (2) optimization of the active emitter-to-absorber area ratio (an additional twofold improvement). Optimizing the area ratio at a fixed optical concentration with a nanophotonic absorber–emitter, experimentally demonstrated in this work, can be easily implemented in future STPV designs to increase overall efficiency.

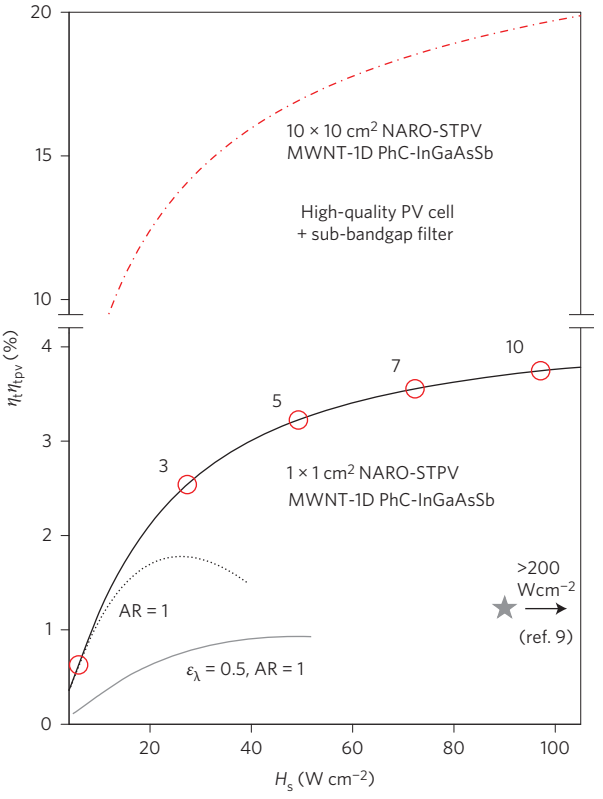

Figure 4 | Relative improvements in efficiency and near-term predictions for NARO-STPVs. Conversion efficiency $\eta_t\eta_{tpv}$ as a function of a solar irradiance H_s. Contributions to $\eta_t\eta_{tpv}$ relative to a greybody absorber–emitter: MWNT-1D PhC absorber–emitter (twofold improvement) and area ratio optimization (additional twofold improvement). Efficiencies approaching 20% were predicted with a scaled-up (10 × 10 cm^2) NARO-STPV utilizing a high-quality 0.55 eV photovoltaic module with a sub-bandgap reflector[20]. All points and predictions were made using the SQ1DD model (H_s was treated as collimated).

From the SQ1DD model, our highest-efficiency operating point corresponds to a temperature of 1,235 K with 54% thermal efficiency and 5.8% TPV efficiency. As the device scales in planar area from 1 × 1 cm^2 to 10 × 10 cm^2 (Fig. 4), the thermal efficiency should improve to ~75% as parasitic losses to the inactive area and mechanical supports decrease from 91% to 20% of the useful emission (Supplementary Fig. 5). Another important aspect limiting our conversion efficiency is the performance of the photovoltaic cell ($V_{oc} = 0.57E_g$, 0.48 fill factor, 83% active area). Using an improved, yet realistic 0.55 eV InGaAsSb cell ($V_{oc} = 0.70E_g$, 0.74 fill factor, 90% active area) and a sub-bandgap photon reflecting filter[26], the STPV efficiency should approach 20% at moderate optical concentrations (Fig. 4). Although this result requires a scale-up of our processing and experimental systems, the present experimental demonstration of a STPV with 1 cm^2 nanophotonic absorber–emitter validates our model. Moreover, the efficiency can be further enhanced through improvements in low-bandgap photovoltaics (such as GaSb, germanium and graphene-based photovoltaics), better spectral control[5,15,21] and higher-temperature operation. Unlike silicon photovoltaic cells that have reached ~85% of their thermodynamic efficiency, the best-performing low-bandgap (TPV) cells exhibit 30–50% of their thermodynamic efficiency[10,25,26,28]. By re-optimizing the geometry of the 1D PhC, our nanophotonic absorber–emitter may be paired with photovoltaic

bandgaps up to ~0.7 eV. Beyond this point, higher-temperature photonic-crystal materials, such as refractory metals[18], are required. The efficiency improvements demonstrated in this work, as well as the promising predictions using a validated model, suggest the viability of nanophotonic STPVs for efficient and scalable solar energy conversion.

Methods

The absorber and emitter were prepared using conventional physical and chemical vapour deposition (PVD, CVD) processes. The polycrystalline silicon and SiO_2 layers of the 1D photonic-crystal emitter were deposited by low-pressure and plasma-enhanced chemical vapour deposition, respectively[6]. The wafer was annealed after each deposition. On the back side of the emitter, a 10 nm adhesion layer of titanium was sputtered on the substrate, followed by a 200 nm layer of tungsten. Using a laser-cut acrylic contact mask, a seed layer for CNT growth was deposited onto the samples with electron-beam evaporation. The CNTs were grown using a high-temperature CVD process in a H_2/He environment by modifying a previously developed procedure[29]. The samples were heated to 720 °C from room temperature in ~10 min and held at 720 °C for 5 min to anneal the iron seed. CNTs were grown for 10 min at 720 °C using an ethylene gas carbon source. All flowing gases were preheated to 625 °C. Following growth, the furnace was rapidly cooled in a H_2/He environment.

The absorber–emitter substrate was mechanically secured using a custom spring-loaded needle-support layout. Vacuum gaps of 400 μm and 300 μm separated the shield from the absorber, and the emitter from the photovoltaic cell, respectively, so that the aperture/absorber and emitter/cell view factors exceeded 0.85. Manual linear stages were used to align and control the spacing between the reflecting shield, the absorber–emitter, and the photovoltaic cell. Experiments were conducted on each absorber–emitter pair at varying levels of flux of simulated solar radiation H_s through the aperture (10–75 W cm^{-2}) by changing the distance between the light source and the experiment (Supplementary section 'Experimental set-up'). H_s is defined as the input solar power through the aperture normalized by the aperture area or, equivalently, the nanotube absorber area. I–V and temperature measurements were obtained at steady operating conditions of the STPV device. Uncertainty in the reported experimental quantities was evaluated based on propagation of the following errors: variance (using a t-distribution with a 95% confidence interval), instrument error and resolution error. The photovoltaic temperature was maintained near 293 K using a chilled water loop (Supplementary equation (S1)).

Received 17 September 2013; accepted 2 December 2013; published online 19 January 2014

References

1. Schwede, J. W. *et al.* Photon-enhanced thermionic emission for solar concentrator systems. *Nature Mater.* **9,** 762–767 (2010).
2. Kraemer, D. *et al.* High-performance flat-panel solar thermoelectric generators with high thermal concentration. *Nature Mater.* **10,** 532–538 (2011).
3. Harder, N.-P. & Würfel, P. Theoretical limits of thermophotovoltaic solar energy conversion. *Semicond. Sci. Technol.* **18,** 151–156 (2003).
4. Shockley, W. & Queisser, H. J. Detailed balance limit of efficiency of p-n junction solar cells. *J. Appl. Phys.* **32,** 510–519 (1961).
5. Rephaeli, E. & Fan, S. Absorber and emitter for solar thermo-photovoltaic systems to achieve efficiency exceeding the Shockley–Queisser limit. *Opt. Express* **17,** 15145–15159 (2009).
6. Chan, W. R. *et al.* Toward high-energy-density, high-efficiency, and moderate-temperature chip-scale thermophotovoltaics. *Proc. Natl Acad. Sci. USA* **110,** 5309–5314 (2013).
7. Datas, A., Chubb, D. L. & Veeraragavan, A. Steady state analysis of a storage integrated solar thermophotovoltaic (SISTPV) system. *Sol. Energ.* **96,** 33–45 (2013).
8. Chubb, D. L., Good, B. S. & Lowe, R. A. Solar thermophotovoltaic (STPV) system with thermal energy storage. *AIP Conf. Proc.* **358,** 181–198 (1996).
9. Datas, A. & Algora, C. Development and experimental evaluation of a complete solar thermophotovoltaic system. *Prog. Photovolt. Res. Appl.* **21,** 1025–1039 (2012).
10. Vlasov, A. S. *et al.* TPV systems with solar powered tungsten emitters. *AIP Conf. Proc.* **890,** 327–334 (2007).
11. Yugami, H., Sai, H., Nakamura, K., Nakagawa, H. & Ohtsubo, H. Solar thermophotovoltaic using Al_2O_3/$Er_3Al_5O_{12}$ eutectic composite selective emitter. *IEEE Photovolt. Spec. Conf.* **28,** 1214–1217 (2000).
12. Chubb, D. L. *Fundamentals of Thermophotovoltaic Energy Conversion* (Elsevier, 2007).
13. Siegel, R. & Howell, J. R. *Thermal Radiation Heat Transfer* (Hemisphere, 1981).
14. Florescu, M. *et al.* Improving solar cell efficiency using photonic band-gap materials. *Sol. Energ. Mat. Sol. C* **91,** 1599–1610 (2007).
15. Bermel, P. *et al.* Design and global optimization of high-efficiency thermophotovoltaic systems. *Opt. Express* **18,** A314–A334 (2010).
16. Ghebrebrhan, M. *et al.* Tailoring thermal emission via Q matching of photonic crystal resonances. *Phys. Rev. A* **83,** 033810 (2011).
17. Rinnerbauer, V. *et al.* Recent developments in high-temperature photonic crystals for energy conversion. *Energy Environ. Sci.* **5,** 8815–8823 (2012).
18. Rinnerbauer, V. *et al.* High-temperature stability and selective thermal emission of polycrystalline tantalum photonic crystals. *Opt. Express* **21,** 11482–11491 (2013).
19. De Zoysa, M. *et al.* Conversion of broadband to narrowband thermal emission through energy recycling. *Nature Photon.* **6,** 535–539 (2012).
20. Celanovic, I., Jovanovic, N. & Kassakian, J. Two-dimensional tungsten photonic crystals as selective thermal emitters. *Appl. Phys. Lett.* **92,** 193101 (2008).
21. Wu, C. *et al.* Metamaterial-based integrated plasmonic absorber/emitter for solar thermo-photovoltaic systems. *J. Opt.* **14,** 024005 (2012).
22. Yang, Z-P., Ci, L., Bur, J. A., Lin, S-Y. & Ajayan, P. M. Experimental observation of an extremely dark material made by a low-density nanotube array. *Nano Lett.* **8,** 446–451 (2008).
23. Yang, Z-P. *et al.* Experimental observation of extremely weak optical scattering from an interlocking carbon nanotube array. *Appl. Opt.* **50,** 1850–1855 (2011).
24. Shi, H., Ok, J. G., Baac, H. W. & Guo, L. J. Low density carbon nanotube forest as an index-matched and near perfect absorption coating. *Appl. Phys. Lett.* **99,** 211103 (2011).
25. Wang, C. A. *et al.* High-quantum-efficiency 0.5 eV GaInAsSb/GaSb thermophotovoltaic devices. *Appl. Phys. Lett.* **75,** 1305–1307 (1999).
26. Dashiell, M. W. *et al.* Quaternary InGaAsSb thermophotovoltaic diodes. *IEEE Trans. Electron.* **53,** 2879–2891 (2006).
27. Chan, W. *et al.* Modeling low-bandgap thermophotovoltaic diodes for high-efficiency portable power generators. *Sol. Energ. Mater. Sol. C* **94,** 509–514 (2010).
28. Posthuma, N. E., van der Heide, J., Flamand, G. & Poortmans, G. Emitter formation and contact realization by diffusion for germanium photovoltaic gevices. *IEEE Trans. Electron.* **54,** 1210–1215 (2007).
29. Nessim, G. D. *et al.* Low temperature synthesis of vertically aligned carbon nanotubes with electrical contact to metallic substrates enabled by thermal decomposition of the carbon feedstock. *Nano Lett.* **9,** 3398–3405 (2009).

Acknowledgements

This work is supported as part of the Solid-State Solar Thermal Energy Conversion (S3TEC) Center, an Energy Frontier Research Center funded by the US Department of Energy, Office of Science, Office of Basic Energy Sciences under DE-FG02-09ER46577. A.L. acknowledges the support of the Martin Family Society, the MIT Energy Initiative and the National Science Foundation GRF. Y.N. acknowledges support from the Basic Science Research Program through the National Research Foundation of Korea (NRF) funded by the Ministry of Science, ICT & Future Planning (no. 2012R1A1A1014845). The authors thank C. Wang from Lincoln Laboratory for providing the InGaAsSb cells; H. Mutha, D. Li and C.V. Thompson's group (for CNT growth); N. Miljkovic, T. Humplik, J. Sack, D. Preston and the Device Research Lab (for SEMs, experimental set-up); and D. Kraemer, M. Luckyanova, G. Chen and the Nanoengineering group (for advice).

Author contributions

All authors contributed extensively to this work. A.L., D.M.B. and Y.N. envisioned and implemented the experimental studies. A.L. and D.M.B. fabricated the absorber, executed the experiments and wrote the paper. W.R.C. designed and fabricated the emitter. I.C., M.S. and E.N.W. supervised and guided the project.

Additional information

Supplementary information is available in the online version of the paper. Reprints and permissions information is available online at www.nature.com/reprints. Correspondence and requests for materials should be addressed to E.N.W.

Competing financial interests

The authors declare no competing financial interests.